Spin pumping in ion-beam sputtered Co_2FeAl/Mo bilayers: Interfacial Gilbert damping

Sajid Husain,[1] Ankit Kumar,[2] Vineet Barwal,[1] Nilamani Behera,[2] Serkan Akansel,[2] Peter Svedlindh,[2] and Sujeet Chaudhary[1,*]
[1]*Thin Film Laboratory, Department of Physics, Indian Institute of Technology Delhi, New Delhi 110016, India*
[2]*Department of Engineering Sciences, Uppsala University, Box 534, SE-751 21 Uppsala, Sweden*

(Received 10 October 2017; revised manuscript received 6 January 2018; published 23 February 2018)

The spin-pumping mechanism and associated interfacial Gilbert damping are demonstrated in ion-beam sputtered Co_2FeAl (CFA)/Mo bilayer thin films employing ferromagnetic resonance spectroscopy. The dependence of the net spin-current transportation on Mo layer thickness, 0 to 10 nm, and the enhancement of the net effective Gilbert damping are reported. The experimental data have been analyzed using spin-pumping theory in terms of spin current pumped through the ferromagnet/nonmagnetic metal interface to deduce the real spin-mixing conductance and the spin-diffusion length, which are estimated to be $1.56(\pm0.30)\times10^{19}$ m^{-2} and $2.61(\pm0.15)$ nm, respectively. The damping constant is found to be $8.8(\pm0.2)\times10^{-3}$ in the Mo(3.5 nm)-capped CFA(8 nm) sample corresponding to an ∼69% enhancement of the original Gilbert damping $5.2(\pm0.6)\times10^{-3}$ in the Al-capped CFA thin film. This is further confirmed by inserting the Cu dusting layer which reduces the spin transport across the CFA/Mo interface. The Mo layer thickness-dependent net spin-current density is found to lie in the range of $1-4$ MAm^{-2}, which also provides additional quantitative evidence of spin pumping in this bilayer thin-film system.

DOI: 10.1103/PhysRevB.97.064420

I. INTRODUCTION

Magnetic damping is an exceedingly important property for spintronic devices due to its influence on power consumption and information writing in the spin-transfer torque (STT) random access memories [1,2]. It is therefore of high importance to study the generation, manipulation, and detection of the flow of spin angular momentum to enable the design of efficient spin-based magnetic memories and logic devices [3]. The transfer of spin angular momentum known as spin pumping in ferromagnetic (FM)/nonmagnetic (NM) bilayers provides information of how the precession of the magnetization transfers spin angular momentum into the adjacent nonmagnetic metallic layer [4]. This transfer (pumping) of spin angular momentum slows down the precession and leads to an enhancement of the effective Gilbert damping constant in FM/NM bilayers. This enhancement has been an area of intensive research since the novel mechanism (theory) of spin pumping was proposed by Brataas *et al.* [5,6]. The amount of spin pumping is quantified by the magnitude of the spin-current density at the FM/NM interface and theoretically [7] described as $\mathbf{J}_S^{\text{eff}} = \frac{\hbar}{4\pi} g_{\text{eff}}^{\uparrow\downarrow}(\mathbf{m} \times \frac{d\mathbf{m}}{dt})$, where $\mathbf{m}$ is the magnetization unit vector, $\mathbf{J}_S^{\text{eff}}$ is the effective spin-current density pumped into the NM layer from the FM layer, and $g_{\text{eff}}^{\uparrow\downarrow}$ is the effective spin-mixing conductance which is determined by the reflection coefficients of conductance channels at the FM/NM interface [5].

To date, a number of NM metals, such as Pt, Au [5], Pd [8,9], β-Ta [10], Ru [11], etc. have been extensively investigated with regard to their performance as spin-sink material when in contact with a FM. It is to be noted here that none of the Pt, Pd, Ru, and Au is an earth-abundant material [12]. Thus, there is a natural need to search for new nonmagnetic materials which could generate large spin current at the FM/NM interface. In this study, we have explored the potential of the transition metal molybdenum (Mo) as a new candidate material for spin pumping owing to the fact that Mo possesses a large spin-orbit coupling [13]. To the best of our knowledge, Mo has not been used to date for the study of spin-pumping effect in a FM/NM bilayer system.

In a FM/NM bilayer and/or multilayer system, there are several mechanisms for dissipation of the spin angular momentum which are categorized as intrinsic and extrinsic. In the intrinsic category, the magnon-electron coupling, i.e., spin-orbit coupling (SOC), contributes significantly [14]. Among the extrinsic category, the two-magnon scattering (TMS) mechanism is linked to the inhomogeneity and interface/surface roughness of the heterostructure, etc. [15–17]. For large SOC, interfacial *d-d* hybridization between the NM and FM layers is highly desirable [16]. Thus, the FM-NM interfacial hybridization is expected to result in enhancement of the transfer of spin angular momentum from the FM to the NM layer, and hence the NM layer can act as a spin reservoir (sink) [18]. But, the NM metallic layer does not always act as a perfect spin reservoir due to the spin accumulation effect which prevents transfer of angular momentum to some extent and as a result, a backflow of spin current towards the FM [6] is estabished. While the flow of spin angular momentum through the FM/NM interface is determined by the effective spin-mixing conductance ($g_{\text{eff}}^{\uparrow\downarrow}$) at the interface, the spin backflow is governed by the spin-diffusion length (λ_d). It is emphasized here that these parameters ($g_{\text{eff}}^{\uparrow\downarrow}$ and λ_d) are primarily tuned by appropriate selection of a suitable NM layer.

In this work, we have performed ferromagnetic resonance (FMR) measurements to explore the spin-pumping phenomenon and associated interfacial Gilbert damping enhancement in the $Co_2FeAl(8\text{ nm})/Mo(t_{Mo})$ bilayer system, t_{Mo} is the thickness of Mo, which is varied from 0 to 10 nm. The

*Corresponding author: sujeetc@physics.iitd.ac.in

t_{Mo}-dependent net spin-current transfer across the interface and spin-diffusion length of Mo are estimated. The choice of employing the Heusler alloy $CoFe_2Al$ (CFA) as a thin FM layer lies in its half metallic character anticipated at room temperature [19,20], a trait which is highly desirable in any spintronic device operating at room temperature.

II. EXPERIMENTAL DETAILS

The CFA thin films with fixed thickness of 8 nm were grown on naturally oxidized Si(100) substrate at 573 K temperature using an ion-beam sputtering deposition system (NORDIKO-3450). The substrate temperature (573 K) has been selected following the growth optimization from our previous reports [21,22]. On the top of the CFA layer, a Mo film with thickness t_{Mo} ($t_{Mo} = 0$, 0.6, 1.0, 1.5, 2.0, 3.0, 4, 5, 7, 8, and 10) was deposited *in situ* at room temperature. In addition, a series of trilayer heterostructure of CFA(8)/Cu(t_{Cu})/Mo(5) ($t_{Cu} =$ 1, 3, 5, 8, and 10) was also prepared to understand and confirm the effect of an additional interface on the Gilbert damping enhancement (spin pumping). To evaluate the real value of the Gilbert damping, in a single-layer CFA, a bilayer CFA(8)/Al(5) was also prepared and studied by FMR measurements. Numbers in parentheses are film thicknesses in nm. All the samples were prepared at a constant working pressure of $\sim 8.5\times10^{-5}$ Torr (base vacuum $\sim 1.0\times10^{-7}$ Torr); Ar gas was directly fed at 4 sccm into the rf-ion source operated at 75W with the deposition rates of 0.03 and 0.02 nm/s for CFA and Mo, respectively. The deposition rate for Cu was 0.07 nm/s at 80 W. The samples were then cut into 1×4 mm^2 to record the FMR spectra employing a homebuilt FMR setup as shown in Fig. 3. The data were collected in dc-magnetic field sweep mode by keeping the microwave frequency fixed. The saturation magnetization was measured using the Quantum Design make Physical Property Measurement System (model PPMS Evercool-II) with the vibrating sample magnetometer option (QD PPMS-VSM). The film density, thickness, and interface/surface roughness were estimated by simulating the specular x-ray reflectivity (XRR) spectra using the PANALYTICAL X'PERT reflectivity software (Version 1.2 with segmented fit). To determine surface morphology/microstructure (e.g., roughness), topographical imaging was performed using the "Bruker dimension ICON scan assist" atomic force microscope (AFM). All measurements were performed at room temperature.

III. RESULTS AND DISCUSSION

A. XRR and AFM: Interface/surface analysis

Figure 1 shows the specular XRR spectra recorded on all the CFA(8)/Mo(t_{Mo}) bilayer thin films. The fitting parameters were accurately determined by simulating (red lines) the experimental curves (filled circles) and are presented in Table I. It is evident that for the smallest NM layer thickness, Mo(0.6), the estimated values of the roughness from XRR and AFM are slightly larger in comparison to the thickness of the Mo layer which indicates that the surface coverage of Mo layer is not enough to cover all of the CFA surface in the CFA(8)/Mo(0.6)

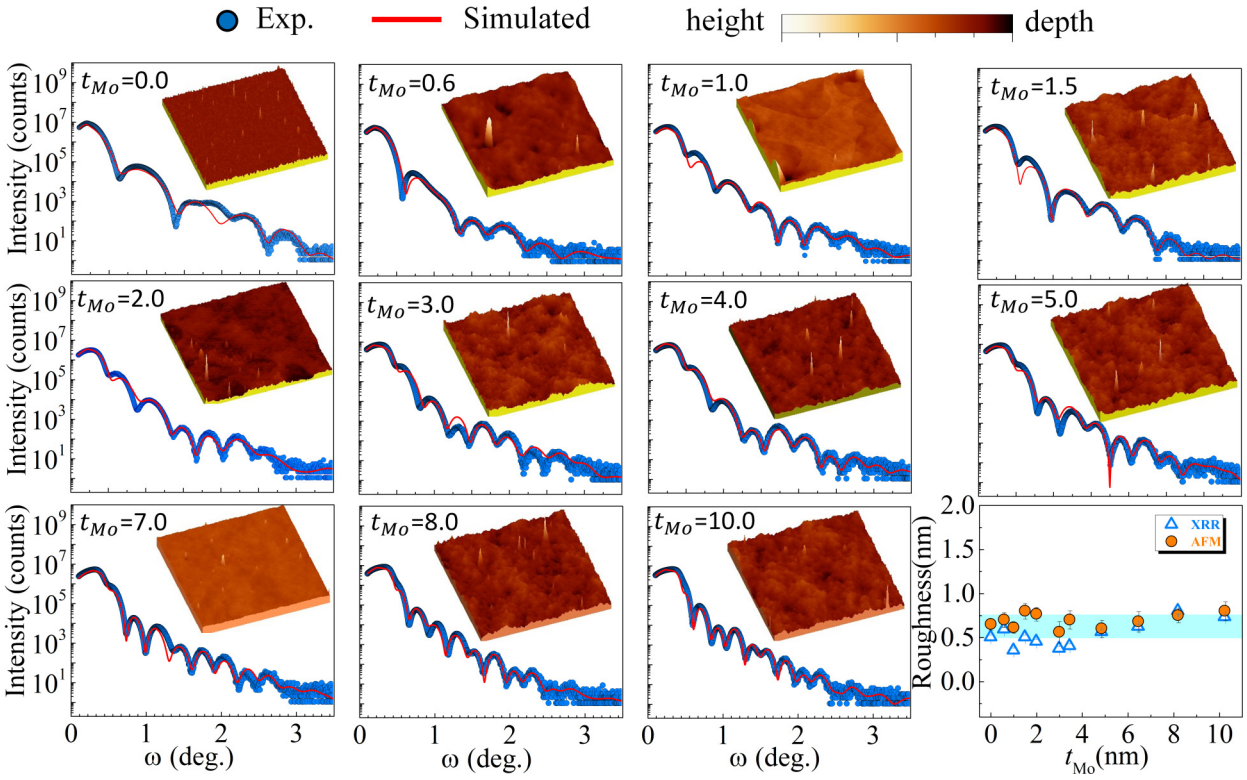

FIG. 1. XRR spectra and the AFM topographical images of CFA(8)/Mo(t_{Mo}). In the respective XRR spectra, circles represent the recorded experimental data points, and lines represent the simulated profiles. The estimated values of the surface roughness in the entire sample series as obtained from XRR and AFM topographical measurements are compared in the lowest right panel. The simulated parameters are presented in Table I. All AFM images were recorded on a scan area of $10\times10\,\mu$m^2.

TABLE I. Summary of XRR simulated parameters, i.e., ρ, t_{FM}, t_{Mo}, and σ for the bilayer thin films [CFA(8)/Mo(t_{Mo})]. Here ρ, t_{FM}, t_{Mo}, and σ refer to the density, thickness, and interface width of the individual layers, respectively.

	CFA (Nominal thickness = 8 nm)			Mo			MoO_x		
S. No.	ρ (gm/cc)	t_{FM} (nm)	σ (nm)	ρ (gm/cc)	t_{Mo} (nm)	σ (nm)	ρ (gm/cc)	t (nm)	σ (nm)
1	7.35(±0.05)	7.00(±0.03)	0.20(±0.02)	06.05(±0.07)	0.58(±0.03)	0.94(±0.02)	4.07(±0.02)	0.97(±0.03)	0.59(±0.03)
2	7.31(±0.04)	8.17(±0.02)	0.35(±0.01)	08.58(±0.07)	1.00(±0.02)	0.54(±0.02)	4.04(±0.04)	0.82(±0.02)	0.35(±0.02)
3	7.50(±0.04)	7.22(±0.03)	0.80(±0.02)	10.50(±0.04)	1.50(±0.01)	0.52(±0.02)	5.00(±0.06)	1.08(±0.04)	0.50(±0.03)
4	7.50(±0.05)	8.18(±0.02)	0.37(±0.01)	09.94(±0.02)	2.00(±0.03)	0.64(±0.03)	4.38(±0.01)	0.85(±0.03)	0.45(±0.02)
5	7.00(±0.03)	7.00(±0.04)	1.00(±0.01)	09.50(±0.02)	3.00(±0.04)	0.60(±0.02)	5.17(±0.06)	1.00(±0.02)	0.37(±0.01)
6	7.00(±0.07)	8.28(±0.02)	0.56(±0.03)	10.45(±0.03)	3.46(±0.02)	0.78(±0.01)	4.38(±0.05)	1.01(±0.01)	0.40(±0.01)
7	7.29(±0.05)	8.00(±0.02)	0.44(±0.02)	09.43(±0.05)	4.86(±0.05)	0.26(±0.02)	6.50(±0.04)	0.98(±0.01)	0.56(±0.03)
8	7.22(±0.06)	7.79(±0.03)	0.98(±0.01)	10.50(±0.03)	6.47(±0.03)	0.67(±0.02)	4.81(±0.03)	1.03(±0.02)	0.62(±0.03)
9	7.00(±0.06)	8.12(±0.01)	0.15(±0.02)	09.29(±0.05)	8.21(±0.01)	0.64(±0.01)	4.00(±0.06)	0.96(±0.01)	0.80(±0.02)
10	7.64(±0.02)	8.00(±0.02)	0.17(±0.01)	09.23(±0.04)	10.26(±0.02)	0.67(±0.02)	5.00(±0.04)	1.17(±0.02)	0.73(±0.01)

bilayer sample [modeled in Fig. 2(a)]. For $t_{Mo} \geqslant 1$ nm, the film roughness is smaller than the thickness [indicating that the Mo layer coverage is uniform as modeled in Figs. 2(b) and 2(c)]. For the thicker layers of Mo ($t_{Mo} \geqslant 5$ nm) the estimated values of the surface roughness as estimated from both XRR and AFM are found to be similar, ∼0.6 nm (cf. the lowest right panel in Fig. 1).

B. FMR study

The FMR spectra were recorded on all samples in 5–11 GHz range of microwave frequencies. The measurement configuration has been drawn in Fig. 3. Figure 4(a) shows the FMR spectra recorded on the CFA(8)/Mo(5) bilayer thin film. The FMR signal (I_{FMR}) was fitted with the derivative of symmetric and antisymmetric Lorentzian functions to extract the line-shape parameters, i.e., resonant field H_r and linewidth ΔH, given by [21,23]

$$I_{FMR} = \frac{\partial(U)}{\partial H} = S\frac{\partial(F_S(H_{ext}))}{\partial H_{ext}} + A\frac{\partial(F_A(H_{ext}))}{\partial H_{ext}}$$
$$= -S\frac{\left(\frac{\Delta H}{2}\right)^2(H_{dc}-H_r)}{\left[(H_{dc}-H_r)^2+\left(\frac{\Delta H}{2}\right)^2\right]^2}$$
$$+ A\frac{\frac{\Delta H}{2}\left[\left(\frac{\Delta H}{2}\right)^2-(H_{dc}-H_r)^2\right]}{\left[(H_{dc}-H_r)^2+\left(\frac{\Delta H}{2}\right)^2\right]^2}, \quad (1)$$

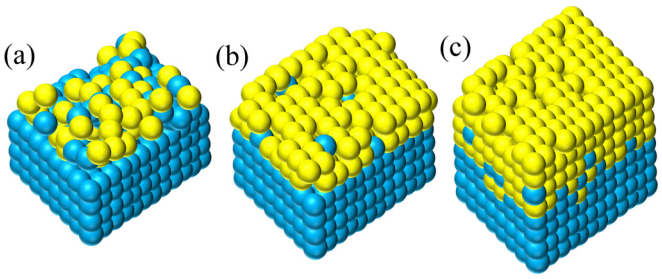

FIG. 2. Atomic representation (model) of the growth of the Mo layer (yellow sphere) on top of the CFA (blue spheres) layer. The film changes from discontinuous to continuous as the thickness of the Mo layer is increased. Shown are the three different growth stages of the films: (a) least coverage, (b) partial coverage, and (c) full coverage.

where $F_S(H_{ext})$ and $F_A(H_{ext})$ are the symmetric and antisymmetric Lorentzian functions, respectively, with S and A being the corresponding coefficients. Here, $H_{ext} = H_{dc} + H_{ac}$. Symbol "$U$" refers to the raw signal voltage from the vector network analyzer (VNA). The linewidth ΔH is the full width at half maximum (FWHM), and H_{dc} is the applied DC-magnetic field.

The f vs $\mu_0 H_r$ plots are shown in Fig. 4(b). In order to calculate the effective magnetization and anisotropy, the experimental results were fitted using the Kittel formula [24]:

$$f = \frac{\mu_0\gamma}{2\pi}\sqrt{(H_r+H_K)(H_r+H_K+M_{eff})}, \quad (2)$$

where $\gamma(=g\mu_B/\hbar)$ is the gyromagnetic ratio with g being the Lande's splitting factor, taken as 2.08 [25], μ_B is the Bohr magneton, $\hbar$ is the reduced Planck's constant, $\mu_0 M_{eff}$ is the effective saturation magnetization, and $\mu_0 H_K$ is the uniaxial anisotropy field. The values of $\mu_0 M_{eff}$ are comparable to the bulk value of $\mu_0 M_S$ (solid line) and the experimentally determined values of $\mu_0 M_S$ (obtained from VSM measurements) as shown in Fig. 4(c). Figure 4(d) shows the $\mu_0 H_r$ vs t_{Mo} behavior at different constant frequencies ranging between 5 and 11 GHz. The observed values of $\mu_0 H_r$ are constant for all the Mo capped layers, which clearly indicates that the dominant contribution to the observed resonance spectra arises from the intrinsic effect, i.e., magnon-electron scattering [26]. Figure 4(e) represents the variation of $\mu_0 H_K$ with t_{Mo} from which the decrease in $\mu_0 H_K$ with increase in t_{Mo} is clearly evident. This observed reduction in $\mu_0 H_K$ could possibly stem from the changes in spin accumulation with increasing t_{Mo} [27].

Further, the FMR spectra were also recorded on CFA(8)/Cu(t_{Cu})/Mo(5) trilayer thin film series for the comparison with the result obtained on the CFA(8)/Mo(5) bilayer. Figure 4(f) displays the $\mu_0 H_r$ vs f for different t_{Cu} from 1 to 10 nm. The variation in the value of $\mu_0 M_{eff}$ is plotted in the inset. It can be seen that $\mu_0 M_{eff}$ does not depend on t_{Cu} and its values are comparable to that found for the CFA(8)/Mo(5) bilayer [solid line, inset Fig. 4(f)]. Figure 5 shows the magnetization hysteresis curves measured at room temperature for the series of trilayer samples having different t_{Cu} (including $t_{Cu} = 0$) to determine the influence of the Cu layer on the saturation magnetization of CFA, if any. It can be

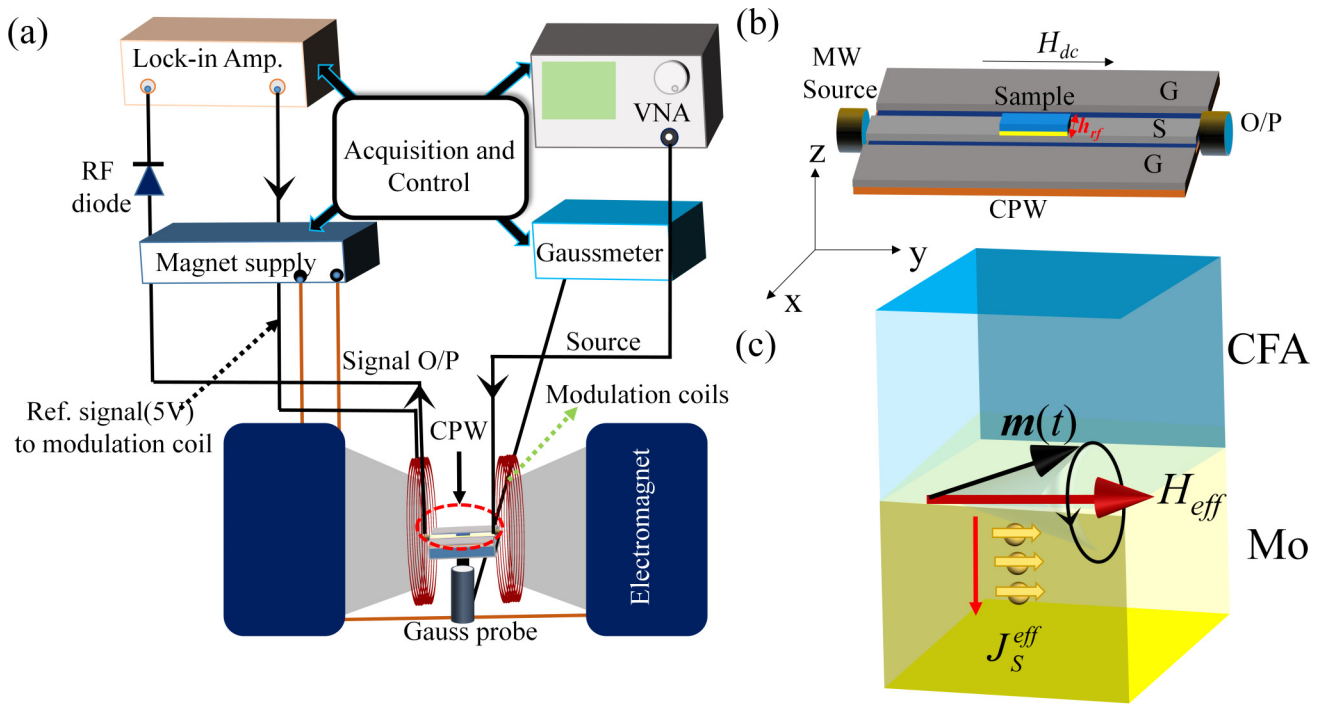

FIG. 3. (a) Schematic illustration of the FMR measurement configuration. (b) The coplanar waveguide on which the sample is placed upside down on the central signal line (S) separated from the ground lines (G). The VNA supplies the microwave (MW) signal through S and the FMR signal, modulated by an ac field (H_{ac}) of 103 A/m amplitude (211.5 Hz), is detected via the rf diode using the lock-in amplifier. (c) Schematic of the CFA/Mo bilayer structure portrayed to illustrate the generation and flow of spin current density J_S^{eff} at the CFA/Mo interface as a result of spin pumping.

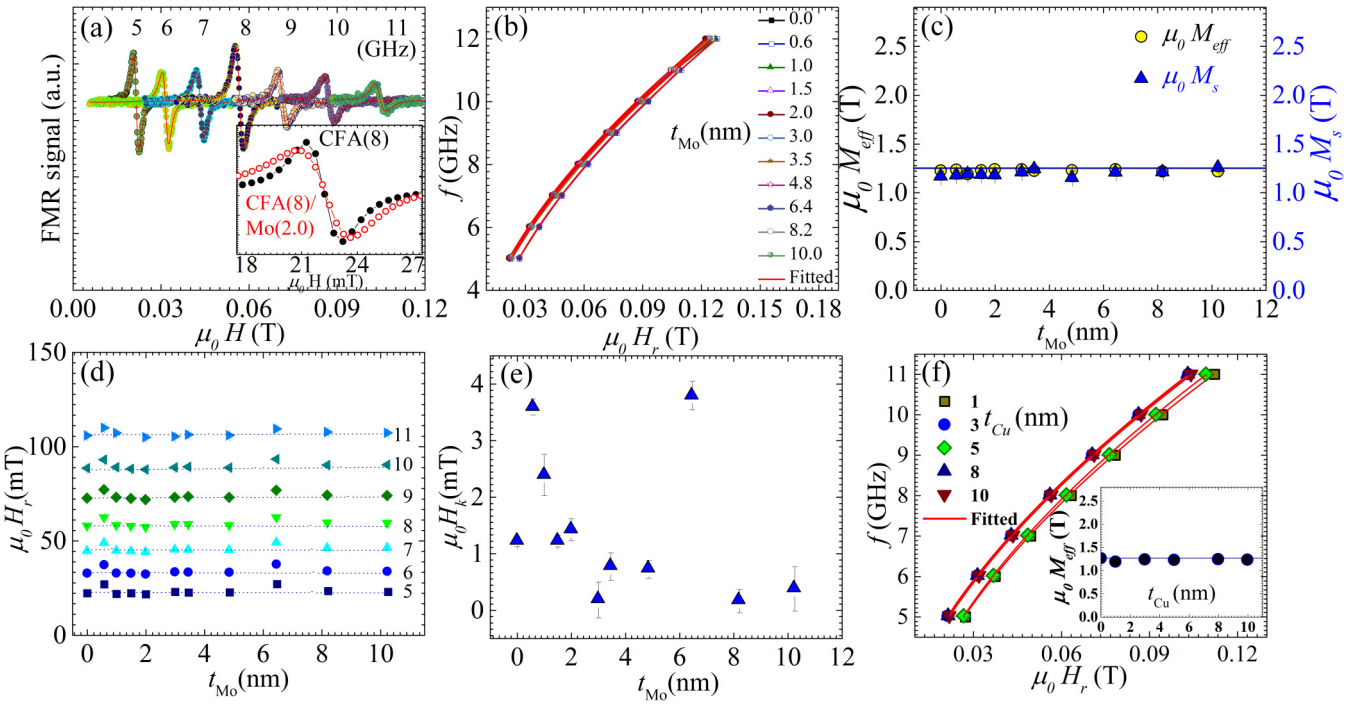

FIG. 4. (a) Typical FMR spectra recorded at various frequencies (numbers in graph are the MW frequencies in GHz) for the CFA(8)/Mo(5) bilayer sample [symbols correspond to experimental data and red lines are fits to Eq. (1)]. Inset: FMR spectra of CFA(8) single-layer (filled circles) and CFA(8)/Mo(2) bilayer (open circles) samples measured at 5 GHz showing the increase in linewidth due to spin pumping. (b) Resonance field $\mu_0 H_r$ vs f for all the samples [red lines are the fits to Eq. (2)]. (c) Effective magnetization (scale on left) and saturation magnetization (scale on right) vs t_{Mo}. The solid line represents the bulk value of the saturation magnetization of Co_2FeAl. (d) Resonance field $\mu_0 H_r$ vs t_{Mo} at different constant frequencies for CFA(8)/Mo(t_{Mo}) bilayer thin films. (e) Anisotropy field $\mu_0 H_K$ vs t_{Mo}. (f) $\mu_0 H_r$ vs f for CFA(8)/Cu(t_{Cu})/Mo(5) trilayer thin films. Inset shows $\mu_0 M_{\text{eff}}$ vs t_{Cu}.

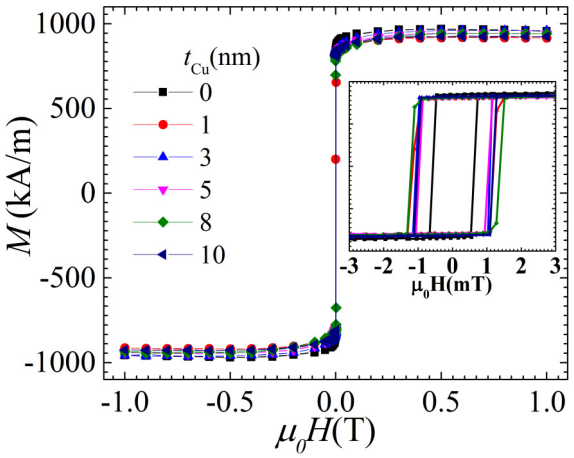

FIG. 5. Magnetization hysteresis (M-H) curves for CFA(8)/Cu(t_{Cu})/Mo(5) trilayers. (Inset: zoomed hysteresis for coercivity.)

seen that the coercivity values in the CFA(8)/Cu(t_{Cu})/Mo(5) samples cover the range between 1.0 and 1.3 mT, values that are relatively higher compared to the value of 0.6 mT in CFA(8)/Mo(5). This increase is attributed to the enhanced surface-pinning contributions due to insertion of the Cu dusting layer [28]. Further, it has been observed that compared to the CFA(8)/Cu(t_{Cu})/Mo(5) trilayer samples, the saturation magnetization is slightly higher in the case of CFA(8)/Mo(5) bilayer (where Mo makes a direct contact to CFA), suggesting the possible existence of a magnetic proximity effect [29–31]. The proximity effect will be addressed in a separate study on different series of multilayers in which CFA is capped with different nonmagnetic layers.

C. Mo thickness-dependent spin pumping

Figure 6(a) shows the linewidth $\mu_0 \Delta H$ vs f (for clarity, the results are shown only for a few selected samples). The frequency-dependent linewidth can mainly have two contributions: the intrinsic magnon-electron scattering contribution and the extrinsic TMS contribution. The extrinsic TMS contribution in linewidth has been analyzed (not presented here) using the methods given by Arias and Mills [32]. A similar analysis was reported in one of our previous studies on the CFA/Ta system [21]. For the present case, the linewidth analysis shows that inclusion of the TMS part does not affect the Gilbert damping, which means the TMS contribution is negligible in our case. It is, however, difficult to exclude this TMS contribution precisely within studied narrow frequency range. Now, the effective Gilbert damping constant α_{eff} can be estimated using

$$\Delta H = \Delta H_0 + \frac{4\pi\, \alpha_{\text{eff}}\, f}{\mu_0\, \gamma} \tag{3}$$

Here, ΔH_0 is the frequency-independent contribution from sample inhomogeneity, while the second term corresponds to the frequency-dependent contribution associated with the intrinsic Gilbert relaxation. Here, α_{eff}, defined as $\alpha_{\text{eff}} = \alpha_{\text{SP}} + \alpha_{\text{CFA}}$, is the effective Gilbert damping which includes the intrinsic value of CFA (α_{CFA}) and a spin-pumping contribution (α_{SP}) from the CFA/Mo bilayer.

The extracted effective Gilbert damping constant values for different t_{Mo} are shown in Fig. 6(b). An enhancement of the Gilbert damping constant with the increase of the Mo layer thickness is clearly observed, which is anticipated owing to the transfer of spin angular momenta by spin pumping from CFA to the Mo layer at the CFA/Mo interface. The value of α_{eff} is found to increase up to $8.8(\pm 0.2)\times 10^{-3}$ with the increase in t_{Mo}, which corresponds to ~69% [compared to the Gilbert damping value of CFA(8)/Al(5)] enhancement of the damping constant due to spin pumping. The Gilbert damping values for uncapped and Al-capped CFA thin films are indicated by the dashed-dotted and dashed lines, respectively, in Fig. 6(b). It is remarkable that such a large change in Gilbert damping is observed for the CFA/Mo bilayer; the change is comparable to those reported when a high-SOC NM such as Pt [8], Pd [33] [9], Ru [11], and Ta [34] is employed in FM/NM bilayers. Here, we would like to mention that the enhancement of the Gilbert damping can, in principle, also be explained by extrinsic TMS contributions in CFA/Mo(t_{Mo}) bilayers by considering the variation of H_r with NM thickness [26]. In our case, the $\mu_0 H_r$ is constant for all t_{Mo} [cf. Fig. 4(d)]. Thus, the extrinsic contribution-induced increase in α_{eff} is negligibly small and hence the enhancement of the damping is dominated by the

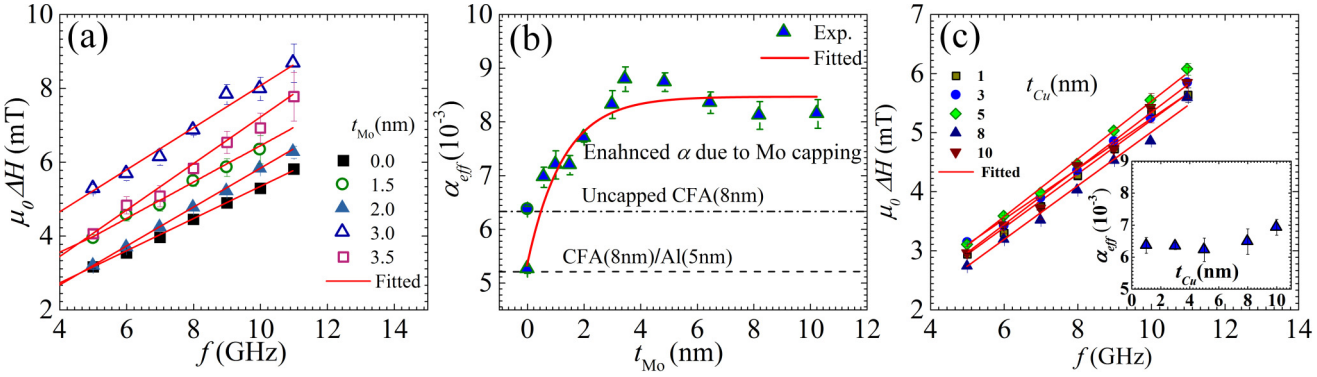

FIG. 6. (a) Linewidth vs frequency for CFA(8)/Mo(t_{Mo}) bilayer thin films. (b) Effective Gilbert damping constant vs Mo layer thicknesses. The dotted-dashed and the dashed lines correspond to uncapped and Al(5) capped CFA layers, respectively. (c) $\mu_0 \Delta H$ vs f plot for CFA(8)/Cu(t_{Cu})/Mo(5) trilayer thin films. Inset shows α_{eff} vs t_{Cu}.

spin-pumping mechanism. The estimated values of $\mu_0 \Delta H_0$ are found to vary from 0.6 to 2.5 mT in the CFA/Mo(t_{Mo}) thin films. The variation in $\mu_0 \Delta H_0$ is assigned to the finite, but small, statistical variations in sputtering conditions between samples with different t_{Mo}.

Further, to affirm the spin pumping in the CFA/Mo bilayer system, trilayer heterostructures were investigated with different thickness (t_{Cu}) of copper dusting layers at the CFA/Mo interface. Figure 6(c) shows a linewidth vs f plot for the CFA(8)/Cu(t_{Cu})/Mo(5) trilayer heterostructures. The Gilbert damping values were found to be approximately constant with minor variations $\alpha_{eff} = 6.3(\pm0.2), 6.3(\pm0.1), 6.2(\pm0.3), 6.4(\pm0.3)$, and $6.9(\pm0.2)\times10^{-3}$ for $t_{Cu} = 1.0$, 3.0, 5.0, 8.0, and 10.0 nm thin layers, respectively. It may be noted that Cu has a very large spin-diffusion length ($\lambda_d \sim 300$ nm) but very weak SOC strength [35,36]. Due to the weak SOC, the asymmetry in the band structure at the FM/Cu interface would thus lead to a nonequilibrium spin accumulation at the CFA/Cu interface [37]. This spin accumulation opposes the transfer of angular momentum into the Mo layer. Further, the change in the effective spin-mixing conductance at Cu interfaces causes a reduced spin pumping. Hence the Gilbert damping value, after insertion of the dusting layer, is found to reduce due to indirect contact with Mo through the Cu layer. The reduction in Gilbert damping/spin pumping with insertion of the interfacial Cu dusting layer is consistent with prior reports on other FM/NM studies [30,37]. It is also known that enhancement of damping in the FM layer (when coupled to the NM layer) can occur due to the magnetic proximity effect [29]. However, we did not find any evidence in favor of the magnetic proximity effect as the saturation magnetization shows a slight decrease on the insertion of the ultrathin Cu(5) dusting layer (Fig. 5) at CFA/Mo bilayer interface, which supports our claim of reduced spin pumping in the CFA/Cu/Mo trilayer samples.

The flow of angular momentum across the FM/NM bilayer interface is determined by the complex spin-mixing conductance $g_{eff}^{\uparrow\downarrow} = \mathrm{Re}(g_{eff}^{\uparrow\downarrow}) + i\ \mathrm{Im}(g_{eff}^{\uparrow\downarrow})$, defined as the flow of angular momentum per unit area through the FM/NM metal interface created by the precessing moments in the FM layer. The term *effective* spin-mixing conductance is being used because it contains the forward and backflow of spin momentum at the FM/NM interface. The imaginary part of the spin-mixing conductance is usually assumed to be negligibly small as compared to the real part [38,39], and therefore, to determine the real part of the spin-mixing conductance, the obtained t_{Mo}-dependent Gilbert damping is fitted with the relation [33]

$$\alpha_{eff} = \alpha_{CFA} + g^{\uparrow\downarrow}\frac{g\mu_B}{4\pi M_S}\frac{1}{t_{CFA}}(1 - e^{(-2t_{Mo})/\lambda_d}), \qquad (4)$$

where α_{CFA} is the damping for a single-layer CFA without Mo capping layer, $g^{\uparrow\downarrow}$ is the real part of spin-mixing conductance which is independent of NM layer thickness and atomic number, and is given in units of m^{-2}, and t_{CFA} is a CFA layer thickness. The exponential term describes the reflection of spin current from the Mo/air interface. Figure 6(b) shows the variation of the effective Gilbert damping constant with t_{Mo} and the fit using Eq. (4) (red line). The values of $g^{\uparrow\downarrow}$ and λ_d (in the Mo layer) are found to be $1.56(\pm0.30)\times10^{19}$ m^{-2} and 2.61(±0.15) nm, respectively. The value of the spin-mixing conductance is comparable to those recently reported in FM/Pt(Pd) thin films such as Co/Pt ($1-4\times10^{19}$ m^{-2}) [8,37], YIG/Pt (9.7×10^{18} m^{-2}) [40], Fe/Pd (1×10^{20} m^{-2}) [9], and Py/Pd(Pt) ($1.4(3.2)\times10^{18}$ m^{-2}) [29].

Since $g^{\uparrow\downarrow}$ does not include the effect of the NM layer, we can therefore evaluate the effective interfacial spin-mixing conductance $g_{eff}^{\uparrow\downarrow}$ which depends on the thickness and the nature of the NM layer as per the following relation [9,41]:

$$g_{eff}^{\uparrow\downarrow}(t_{Mo}) = g^{\uparrow\downarrow}\left[1 + \left[\sqrt{\frac{4\varepsilon}{3}}\tanh\frac{t_{Mo}}{\lambda_d}\right]^{-1}\right]^{-1}, \qquad (5)$$

where $\varepsilon = (Z\,e^2/\hbar\,c)^4$ is a material-dependent parameter (Z is the atomic number of Mo i.e., 42, e is electron charge, and c is the speed of light) whose value for Mo is 0.0088 by using the fundamental constants. The second bracketed term in the above equation describes the effect of the Mo layer on the total interfacial spin-mixing conductance. This factor also includes the effect of spin accumulation at the interface which leads to the spin backflow and the contribution of this term does not become zero at any thickness of the NM layer [41]. Thus, Eq. (5) provides the elemental dependency in calculating the intrinsic interfacial spin-mixing conductance. Using Eq. (5), values of $g_{eff}^{\uparrow\downarrow}(t_{Mo})$ have been computed for various t_{Mo}; the results are shown in Fig. 7. In comparison to results obtained in the previous section [cf. Eq. (4) and Fig. 6(b)] where the $g^{\uparrow\downarrow}$ was assumed to be independent of the effect of NM, the t_{Mo} dependence of $g_{eff}^{\uparrow\downarrow}(t_{Mo})$ as shown in Fig. 7 clearly suggests that the spin-mixing conductance critically depends on the NM layer and its properties. For these bilayers with $t_{Mo} \geqslant 6$ nm, $g_{eff}^{\uparrow\downarrow}(t_{Mo})$ attains its saturation value, which is quite comparable with those reported for Pd and Pt [29,40]. Understandably, such a large value of the spin-mixing conductance will yield a large spin current into the adjacent NM layer [6,7,37,40]. In the next section, we have estimated the spin-current density from the experimental FMR data and discussed the same with regard to spin pumping in further detail.

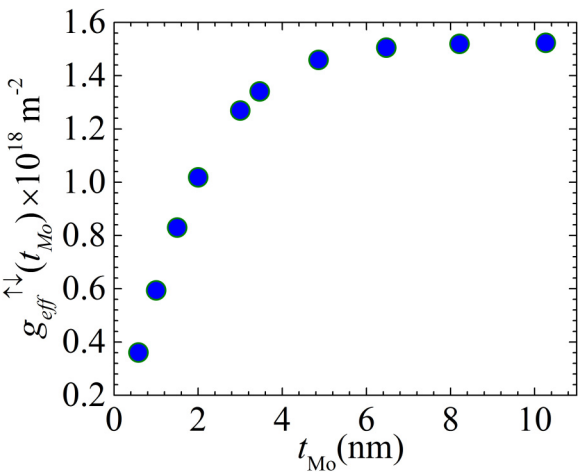

FIG. 7. Effective interfacial spin-mixing conductance vs t_{Mo} of the CFA(8)/Mo(t_{Mo}) bilayers evaluated using Eq. (5).

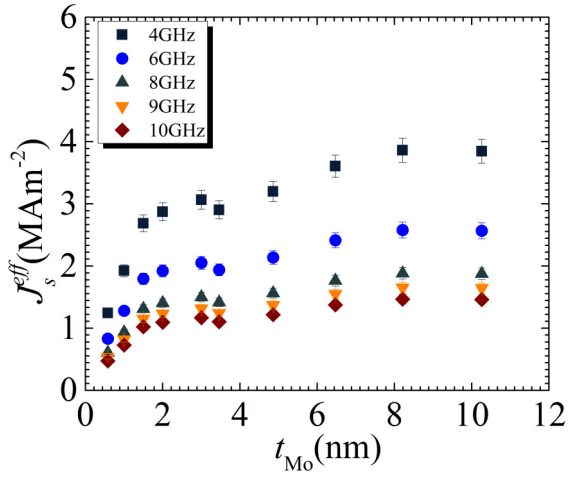

FIG. 8. Effective spin-current density (generated in Mo) vs t_{Mo} at different microwave frequencies calculated using Eq. (6).

D. Spin-current generation in Mo due to spin pumping

The enhancement of the Gilbert damping observed in the CFA(8)/Mo(t_{Mo}) bilayers [Fig. 6(b)] is generally interpreted in terms of the spin current generated in a Mo layer by the spin-pumping mechanism at the bilayer interface [Fig. 3(c)]. The associated net effective spin-current density in Mo is described by the relation [41,42]

$$J_S^{\text{eff}}(t_{\text{Mo}}) = g_{\text{eff}}^{\uparrow\downarrow}(t_{\text{Mo}})\,\frac{2e}{\hbar}\,\frac{\gamma^2\hbar(\mu_0 h_{rf})^2}{8\pi\,\alpha_{\text{eff}}^2} \times\left[\frac{\mu_0\gamma M_{\text{eff}}+\sqrt{(\mu_0\gamma M_{\text{eff}})^2+4\omega^2}}{(\mu_0\gamma M_{\text{eff}})^2+4\omega^2}\right], \quad (6)$$

where $\omega = 2\pi f$ and h_{rf} is the rf field (26 A/m) in the strip line of our coplanar waveguide. $g_{\text{eff}}^{\uparrow\downarrow}(t_{\text{Mo}})$ is the net effective interfacial spin-mixing conductance discussed in the previous section (Fig. 7). The estimated values of $J_S^{\text{eff}}(t_{\text{Mo}})$ for different microwave frequencies are shown in Fig. 8. It is clearly observed that the spin-current density increases with the increase in t_{Mo}, the increase becomes relatively less at higher t_{Mo}, which indicates the progressive spin-current generation in Mo. Such an appreciable change in current density directly provides evidence of the interfacial enhancement of the Gilbert damping in these CFA/Mo bilayers.

Further, it would be interesting to investigate the effect on the spin-current generation in a Mo layer if an ultrathin dusting layer of Cu is inserted at the CFA/Mo interface. In principle, on insertion of a thin Cu layer, the spin pumping should cease because of the unmatched band between the CFA/Mo interfaces owing to the insignificant SOC in Cu. This is in consonance with the observed decrease in Gilbert damping [cf. Fig. 6(c) and associated discussion]. The spin-mixing conductance of the trilayer heterostructure can be evaluated by $\Delta\alpha_{\text{sp}} = g\mu_B g^{\uparrow\downarrow}/\mu_0 M_S t_{\text{CFA}}$ [33], where $\Delta\alpha_{\text{sp}} = \alpha_{\text{eff}} - \alpha_{\text{CFA}}$ is the spin-pumping-induced Gilbert damping contribution, which for the CFA/Cu/Mo(5) trilayer is quite small, i.e., $9.8(\pm0.2)\times10^{-4}$ after Cu(5) insertion. For this trilayer, $g^{\uparrow\downarrow}$ and $g_{\text{eff}}^{\uparrow\downarrow}$ for CFA/Cu(5)/Mo(5) are found to be $4.9(\pm0.11)\times10^{18}\,\text{m}^{-2}$ and $4.58(\pm0.15)\times10^{17}\,\text{m}^{-2}$, respectively, which are *smaller* by a factor of ∼3 compared to that of the CFA/Mo bilayers. Furthermore, using the values of $g_{\text{eff}}^{\uparrow\downarrow}$, $\mu_0 M_{\text{eff}}$, and α_{eff} for the CFA/Cu(5)/Mo(5) trilayer heterostructure in Eq. (6) and for $f = 9$ GHz, the spin-current density is found to be $0.832(\pm0.002)\,\text{MA/m}^2$, which is smaller than that in the CFA/Mo(5) bilayers (cf. Fig. 8). This reduction in α_{eff} and J_S^{eff} subsequent to Cu dusting is quite comparable to previously reported results [37,43]. Reduction in Gilbert damping constant and spin-current density with Cu insertion indeed signifies the correlation between the spin-orbit coupling and the enhancement of Gilbert damping, i.e., spin pumping in these CFA/Mo bilayers.

IV. CONCLUSIONS

We have systematically investigated the changes in the spin dynamics in the ion-beam sputtered Co_2FeAl (CFA)/Mo(t_{Mo}) bilayers for various t_{Mo} at constant CFA thickness of 8 nm. Increasing the Mo layer thickness to its spin-diffusion length, CFA(8)/Mo($t_{\text{Mo}} = \lambda_d$), the effective Gilbert damping constant increases to $8.8(\pm0.2)\times10^{-3}$ which corresponds to about ∼69% enhancement with respect to the α_{eff} value of $5.2(\pm0.6)\times10^{-3}$ for the Al-capped CFA layer (i.e., without the top Mo layer). We interpret our results based on the spin-pumping effects, wherein the effective spin-mixing conductance and spin-diffusion length are found to be $1.56(\pm0.30)\times10^{19}\,\text{m}^{-2}$ and $2.61(\pm0.15)$ nm, respectively. The spin pumping is further confirmed by inserting the Cu layer at the CFA/Mo interface. The overall effect of the damping constant enhancement observed when Mo is deposited over CFA is remarkably comparable to the far less-abundant nonmagnetic metals that are currently being used for spin-pumping applications. From this viewpoint, the demonstration of the material, i.e., Mo, as a suitable spin-pumping medium is indispensable for the development of novel STT spintronic devices.

ACKNOWLEDGMENTS

S.H. acknowledges the Department of Science and Technology, Government of India for providing the INSPIRE Fellowship (IF140093). We acknowledge the financial grants 1(1)/2004-M&C, 1(14)/2007/M&C, and 20(13)/2007-NANO from Department of Information Technology, Government of India. MHRD is also acknowledged for PPMS facility. This work was in part also supported by Knut and Alice Wallenberg (KAW) Foundation Grant No. KAW 2012.0031.

[1] W. Kang, Z. Wang, H. Zhang, S. Li, Y. Zhang, and W. Zhao, in *Proceedings of the Great Lakes Symposium on VLSI 2017* (ACM Press, New York, 2017), pp. 299–304.

[2] E. Eken, I. Bayram, Y. Zhang, B. Yan, W. Wu, and Y. Chen, Integr. VLSI J. **58**, 253 (2017).

[3] S. Bhatti, R. Sbiaa, A. Hirohata, H. Ohno, S. Fukami, and S. N. Piramanayagam, Mater. Today **20**, 530 (2017).

[4] Y. Tserkovnyak, A. Brataas, and G. E. W. Bauer, Phys. Rev. Lett. **88**, 117601 (2002).

[5] A. Brataas, Y. Tserkovnyak, G. E. W. Bauer, and B. I. Halperin, Phys. Rev. B **66**, 060404(R) (2002).

[6] Y. Tserkovnyak, A. Brataas, and G. E. W. Bauer, Phys. Rev. B **66**, 224403 (2002).

[7] Y. Tserkovnyak, A. Brataas, G. E. W. Bauer, and B. I. Halperin, Rev. Mod. Phys. **77**, 1375 (2005).

[8] S. Azzawi, A. Ganguly, M. Tokaç, R. M. Rowan-Robinson, J. Sinha, A. T. Hindmarch, A. Barman, and D. Atkinson, Phys. Rev. B **93**, 054402 (2016).

[9] A. Kumar, S. Akansel, H. Stopfel, M. Fazlali, J. Åkerman, R. Brucas, and P. Svedlindh, Phys. Rev. B **95**, 064406 (2017).

[10] E. Barati and M. Cinal, Phys. Rev. B **95**, 134440 (2017).

[11] H. Yang, Y. Li, and W. E. Bailey, Appl. Phys. Lett. **108**, 242404 (2016).

[12] G. B. Haxel, J. B. Hedrick, and G. J. Orris, *United States Geological Survey Fact Sheet 087-02* (2002).

[13] J. R. Clevelandj and J. L. Stanford, Phys. Rev. Lett. **24**, 1482 (1970).

[14] M. C. Hickey and J. S. Moodera, Phys. Rev. Lett. **102**, 137601 (2009).

[15] M. D. Stiles and A. Zangwill, Phys. Rev. B **66**, 014407 (2002).

[16] J. O. Rantschler, R. D. McMichael, A. Castillo, A. J. Shapiro, W. F. Egelhoff, B. B. Maranville, D. Pulugurtha, A. P. Chen, and L. M. Connors, J. Appl. Phys. **101**, 033911 (2007).

[17] K. Lenz, H. Wende, W. Kuch, K. Baberschke, K. Nagy, and A. Jánossy, Phys. Rev. B **73**, 144424 (2006).

[18] A. Brataas, Y. V. Nazarov, and G. E. W. Bauer, Phys. Rev. Lett. **84**, 2481 (2000).

[19] I. Galanakis, P. H. Dederichs, and N. Papanikolaou, Phys. Rev. B **66**, 174429 (2002).

[20] A. Kumar, F. Pan, S. Husain, S. Akansel, R. Brucas, L. Bergqvist, S. Chaudhary, and P. Svedlindh, Phys. Rev. B **96**, 224425 (2017).

[21] S. Husain, S. Akansel, A. Kumar, P. Svedlindh, and S. Chaudhary, Sci. Rep. **6**, 28692 (2016).

[22] S. Husain, A. Kumar, S. Akansel, P. Svedlindh, and S. Chaudhary, J. Magn. Magn. Mater. **442**, 288 (2017).

[23] L. H. Bai, Y. S. Gui, A. Wirthmann, E. Recksiedler, N. Mecking, C.-M. Hu, Z. H. Chen, and S. C. Shen, Appl. Phys. Lett. **92**, 032504 (2008).

[24] C. Kittel, Phys. Rev. **73**, 155 (1948).

[25] M. Belmeguenai, H. Tuzcuoglu, M. S. Gabor, T. Petrisor, C. Tiusan, D. Berling, F. Zighem, T. Chauveau, S. M. Cherif, and P. Moch, Phys. Rev. B **87**, 184431 (2013).

[26] N. Behera, A. Kumar, S. Chaudhary, and D. K. Pandya, RSC Adv. **7**, 8106 (2017).

[27] S. P. Chen and C. R. Chang, Phys. Status Solidi **244**, 4398 (2007).

[28] S. S. Ahmad, W. He, Y. S. Zhang, J. Tang, Q. Gul, X. Q. Zhang, and Z. H. Cheng, AIP Adv. **6**, 115101 (2016).

[29] M. Caminale, A. Ghosh, S. Auffret, U. Ebels, K. Ollefs, F. Wilhelm, A. Rogalev, and W. E. Bailey, Phys. Rev. B **94**, 014414 (2016).

[30] Y. Sun, H. Chang, M. Kabatek, Y.-Y. Song, Z. Wang, M. Jantz, W. Schneider, M. Wu, E. Montoya, B. Kardasz, B. Heinrich, S. G. E. te Velthuis, H. Schultheiss, and A. Hoffmann, Phys. Rev. Lett. **111**, 106601 (2013).

[31] J. Okabayashi, T. Koyama, M. Suzuki, M. Tsujikawa, M. Shirai, and D. Chiba, Sci. Rep. **7**, 46132 (2017).

[32] R. Arias and D. L. Mills, Phys. Rev. B **60**, 7395 (1999).

[33] J. M. Shaw, H. T. Nembach, and T. J. Silva, Phys. Rev. B **85**, 054412 (2012).

[34] G. Allen, S. Manipatruni, D. E. Nikonov, M. Doczy, and I. A. Young, Phys. Rev. B **91**, 144412 (2015).

[35] S. Yakata, Y. Ando, T. Miyazaki, and S. Mizukami, Jpn. J. Appl. Phys. **45**, 3892 (2006).

[36] S. Mizukami, Y. Ando, and T. Miyazaki, Phys. Rev. B **66**, 104413 (2002).

[37] J.-C. Rojas-Sanchez, N. Reyren, P. Laczkowski, W. Savero, J.-P. Attane, C. Deranlot, M. Jamet, J.-M. George, L. Vila, and H. Jaffres, Phys. Rev. Lett. **112**, 106602 (2014).

[38] K. Xia, P. J. Kelly, G. E. W. Bauer, A. Brataas, and I. Turek, Phys. Rev. B **65**, 220401(R) (2002).

[39] W. Zhang, W. Han, X. Jiang, S.-H. Yang, and S. S. P. Parkin, Nat. Phys. **11**, 496 (2015).

[40] M. Haertinger, C. H. Back, J. Lotze, M. Weiler, S. Geprägs, H. Huebl, S. T. B. Goennenwein, and G. Woltersdorf, Phys. Rev. B **92**, 054437 (2015).

[41] H. Nakayama, K. Ando, K. Harii, T. Yoshino, R. Takahashi, Y. Kajiwara, K. Uchida, Y. Fujikawa, and E. Saitoh, Phys. Rev. B **85**, 144408 (2012).

[42] K. Ando, S. Takahashi, J. Ieda, Y. Kajiwara, H. Nakayama, T. Yoshino, K. Harii, Y. Fujikawa, M. Matsuo, S. Maekawa, and E. Saitoh, J. Appl. Phys. **109**, 103913 (2011).

[43] T. Nan, S. Emori, C. T. Boone, X. Wang, T. M. Oxholm, J. G. Jones, B. M. Howe, G. J. Brown, and N. X. Sun, Phys. Rev. B **91**, 214416 (2015).